Stu2 uses a 15-nm parallel coiled coil for kinetochore localization and concomitant regulation of the mitotic spindle

Karen P. Haase[a,b,c,†], Jaime C. Fox[a,c,†], Amy E. Byrnes[b,c,†], Rebecca C. Adikes[d,†], Sarah K. Speed[d], Julian Haase[d], Brandon Friedman[d], Diana M. Cook[d], Kerry Bloom[d], Nasser M. Rusan[b], and Kevin C. Slep[d,*]

[a]Molecular and Cellular Biophysics Program, [c]Department of Biochemistry and Biophysics, and [d]Department of Biology, University of North Carolina, Chapel Hill, NC 27599; [b]Cell Biology and Physiology Center, National Heart, Lung, and Blood Institute, National Institutes of Health, Bethesda, MD 20892

ABSTRACT **XMAP215/Dis1 family proteins are potent microtubule polymerases, critical for mitotic spindle structure and dynamics. While microtubule polymerase activity is driven by an N-terminal tumor overexpressed gene (TOG) domain array, proper cellular localization is a requisite for full activity and is mediated by a C-terminal domain. Structural insight into the C-terminal domain's architecture and localization mechanism remain outstanding. We present the crystal structure of the *Saccharomyces cerevisiae* Stu2 C-terminal domain, revealing a 15-nm parallel homodimeric coiled coil. The parallel architecture of the coiled coil has mechanistic implications for the arrangement of the homodimer's N-terminal TOG domains during microtubule polymerization. The coiled coil has two spatially distinct conserved regions: CRI and CRII. Mutations in CRI and CRII perturb the distribution and localization of Stu2 along the mitotic spindle and yield defects in spindle morphology including increased frequencies of mispositioned and fragmented spindles. Collectively, these data highlight roles for the Stu2 dimerization domain as a scaffold for factor binding that optimally positions Stu2 on the mitotic spindle to promote proper spindle structure and dynamics.**

Monitoring Editor
Gero Steinberg
University of Exeter

Received: Jan 23, 2017
Revised: Oct 10, 2017
Accepted: Nov 22, 2017

INTRODUCTION

Stu2 is a yeast member of the XMAP215/Dis1 microtubule polymerase family (Gard and Kirschner, 1987). It was isolated in a screen for suppressors of a cold sensitive β-tubulin (*tub2*) mutation that caused a defect in mitotic spindle formation (Wang and Huffaker, 1997). Its depletion leads to reduced cytoplasmic microtubule dynamics, increasing the pause state and decreasing the frequencies of catastrophe and rescue (Kosco *et al.*, 2001). During mitosis, Stu2 localizes at kinetochores and spindle pole bodies and along the mitotic spindle itself (Chen *et al.*, 1998; Usui *et al.*, 2003; Gandhi *et al.*, 2011). Its activity is required for kinetochore microtubule dynamics and stability, centromere positioning, and anaphase spindle elongation (He *et al.*, 2001; Kosco *et al.*, 2001; Severin *et al.*, 2001; Pearson *et al.*, 2003).

XMAP215/Dis1 family members have a multi-domain architecture. Nonyeast members contain an array of three to five N-terminal tubulin-binding tumor overexrpessed gene (TOG) domains, a basic linker, and a C-terminal microtubule plus-end tracking domain that are collectively used to position the polymerase and drive microtubule polymerization (Gard *et al.*, 2004; Brittle and Ohkura, 2005; van der Vaart *et al.*, 2011; Li *et al.*, 2012). In contrast, yeast family members contain only two N-terminal TOG domains, a central basic linker, and a unique C-terminal dimerization domain predicted to be a coiled coil (Nabeshima *et al.*, 1995; Nakaseko *et al.*, 1996; Wang and Huffaker, 1997; Garcia *et al.*, 2001; Al-Bassam *et al.*, 2006). Stu2

This article was published online ahead of print in MBoC in Press (http://www.molbiolcell.org/cgi/doi/10.1091/mbc.E17-01-0057) on November 29, 2017.

†These authors contributed equally.

K.P.H. and K.C.S. conceived the research; K.P.H., A.E.B., J.C.F., R.C.A., B.F., D.C., and K.C.S. collected data; all authors analyzed data; and K.P.H., A.E.B., J.C.F., R.C.A., and K.C.S. wrote the article. All authors commented on the article.

*Address correspondence to: Kevin C. Slep (kslep@bio.unc.edu).

Abbreviations used: ASA, accessible surface area; β-ME, β-mercaptoethanol; BSA, buried surface area; CD, circular dichroism; CR, conserved region; SEC-MALS, size exclusion chromatography–multi-angle light scattering; SeMet, selenomethionine; WT, wild type.

microtubule polymerase activity is dimerization dependent and functionally operates with a pair of two TOG domains (four total). The orientation of the coiled coil (parallel vs. antiparallel) puts mechanistic restrictions on how these four TOG domains collectively engage tubulin subunits to promote their polymerization. The orientation of the coiled coil and whether it plays a role in Stu2 localization and polymerase function remains to be determined.

We present the crystal structure of the Stu2 coiled coil ($Stu2_{CC}$) that reveals a 15-nm-long parallel coiled coil. The coiled coil has two conserved, surface exposed regions. Mutating determinants in either conserved region compromises yeast growth rates under conditions that stress microtubules. Mutations in these conserved regions affect Stu2 spindle localization and compromise spindle structure and dynamics. This work establishes distance constraints for the dimer's N-terminal TOG domains, unveils roles for the coiled coil in proper Stu2 spindle localization, and implicates determinants along the coiled coil as spindle factor binding sites.

RESULTS

The Stu2 conserved C-terminal domain is a homodimeric α-helical domain

The Stu2 C-terminal domain is conserved across yeast species, is predicted to be a coiled coil (Figures 1, A and B), and is required for full Stu2-dependent activity (Al-Bassam *et al.*, 2006). We used size exclusion chromatography–multi-angle light scattering (SEC-MALS) to determine the oligomeric state of the Stu2 C-terminal domain. $Stu2_{CC}$ (residues 655–760) eluted off the gel filtration column as a single homodimeric peak (experimental mass: 27.6 kDa, formula weight: 13.5 kDa; Figure 1C). This agrees with previous studies showing that full-length Stu2 is dimeric and that the Stu2 C-terminal domain is necessary for oligomerization (De Wulf *et al.*, 2003; van Breugel *et al.*, 2003; Al-Bassam *et al.*, 2006).

We next analyzed $Stu2_{CC}$ using circular dichroism (CD). The CD spectrum showed minima at 208 and 222 nm, indicative of α-helical secondary structure (Figure 1D). Thermal melt analysis revealed that $Stu2_{CC}$ melted cooperatively with an inflection point at 51.5°C (apparent T_m), indicative of a relatively stable structure (Figure 1E).

$Stu2_{CC}$ is a 15-nm parallel coiled coil

To determine the structure of $Stu2_{CC}$, we crystallized selenomethionine-substituted $Stu2_{CC}$ and collected 2.5-Å-resolution single-wavelength anomalous dispersion data. Crystals belonged to the space group $P2_1$ and contained two protein molecules in the asymmetric unit that formed a single homodimeric coiled coil. The $Stu2_{CC}$ structure was built and refined to R and R_{free} values of 25.7 and 29.2, respectively. Crystallographic statistics are presented in Supplemental Table S1.

The $Stu2_{CC}$ domain forms a parallel coiled coil over 99 residues (amino acids 657–755) that spans 14.8 nm (Figure 1F). The dimerization interface buries 2670 $Å^2$ of solvent accessible surface area from each chain and involves van der Waals contacts as well as hydrogen bond networks. The domain has a left-handed super-coil that rotates each helix ~270° about the coiled coil's axis. Cortexillin I is the most similar structure currently available in the Protein Data Bank (PDB) (Dali server: 2.3 Å rmsd over 99 aligned Cα atoms, $Z = 7.8$, PDB 1D7M; Burkhard *et al.*, 2000; Holm and Rosenström, 2010). Our structure confirms the homodimeric nature of the Stu2 coiled coil.

$Stu2_{CC}$ has two distinct conserved regions

We next mapped conservation (as delineated in Figure 1B) and electrostatics on the $Stu2_{CC}$ structure. Two distinct areas of conservation were apparent: conserved region I (CRI), spanning residues 671–682, and conserved region II (CRII), spanning residues 702–745 (Figure 1G). $Stu2_{CC}$'s electrostatic profile is polarized with a basic region concentrated within the N-terminal half of the coiled coil and an acidic region concentrated at the domain's C-terminal region (Figure 1H). The coiled coil's N-terminal basic region abuts a positively charged linker (not present in the structure) that bridges TOG2 and the coiled coil and is involved in microtubule binding (Wang and Huffaker, 1997; Al-Bassam *et al.*, 2006). The electrostatic surfaces of CRI and CRII are interspersed with hydrophobic content, suggesting that factors that engage these regions would bind using electrostatic interactions and van der Waals contacts.

At CRI, the Stu2 coiled coil locally flares, deviating significantly from canonical coiled-coil structure (Figure 2A, cyan box). The closest approach of equivalent Cα atoms along a coiled coil occurs at heptad repeat positions *a*–*a*′ and *d*–*d*′ (Figure 2B). Analysis of the *a* and *d* Cα–Cα′ interchain distances across residues 661–755 revealed a flare spanning residues E675–L685 (Figure 2C). Within this region, the conserved tryptophan W678 is packed at the dimerization interface. W678 and W678′ adopt distinct rotameric states and are rotated 180° relative to one another. This positions each tryptophan's indole ring amine on the same face of the coiled coil (Figure 2D). While most of the coiled coil has approximate twofold symmetry, the asymmetric packing of W678 and W678′ creates local asymmetry. The asymmetry generates nonequivalent surfaces on each side of CRI which may limit the stoichiometry or binding affinity of factors that engage CRI.

$Stu2_{CC}$ CRII also displays a number of unique features. The first feature spans residues E702–R707 and involves a network of hydrogen bonds at the dimerization interface (Figure 2, A, green box, and E). At the interface, the asparagine N703 and N703′ side-chain amide groups are oppositely oriented and interact through a hydrogen bond between the N703 Oδ and the N703′ Nδ. Flanking these residues are the arginine-glutamate perimeter pairs R707–E702′ and R707′–E702. The complementary arginine and glutamate residues are differentially positioned to pair and stabilize each respective N703 residue. A second highly conserved feature within CRII is the sequence LRSKE (residues 724–728; Figures 1B and 2, A, yellow box, and F). While L724 and the aliphatic portion of the K727 side chain are positioned at the dimerization interface, R725, S726, E728, and the K727 side-chain amine are solvent accessible and are not involved in intra- or interhelical stabilization. The surface accessibility of these residues suggests that they are involved in factor binding.

The $Stu2_{CC}$ structure does not contain an apparent consensus trigger sequence found in many coiled coils that initiates coiled-coil formation (Burkhard *et al.*, 2000; Kammerer *et al.*, 1998; Steinmetz *et al.*, 1998). Trigger sequences employ intra- and interhelical hydrogen bonding to promote autonomous, regional helical folding, and concomitant homodimerization. The element that triggers $Stu2_{CC}$ coiled-coil formation remains to be determined.

Mutations in $Stu2_{CC}$ CRI and CRII yield growth defects under conditions that stress microtubules

We designed targeted point mutations at the STU2 genomic locus in CRI and CRII to test the role of these regions in Stu2 function. A W678L mutation in CRI (Stu2 CRI^{mut}) replaced the tryptophan with leucine, a residue common to coiled-coil interfaces. In a separate strain, a double R725E, S726A mutation in CRII (Stu2 $CRII^{mut}$) was introduced (see Supplemental Table S2 for strain details). The viability of these strains contrasts with the lethality caused by *stu2* deletion (Wang and Huffaker, 1997). We analyzed the ability of the *stu2* strains to grow under normal growth conditions and under conditions that stress the microtubule cytoskeleton: decreased

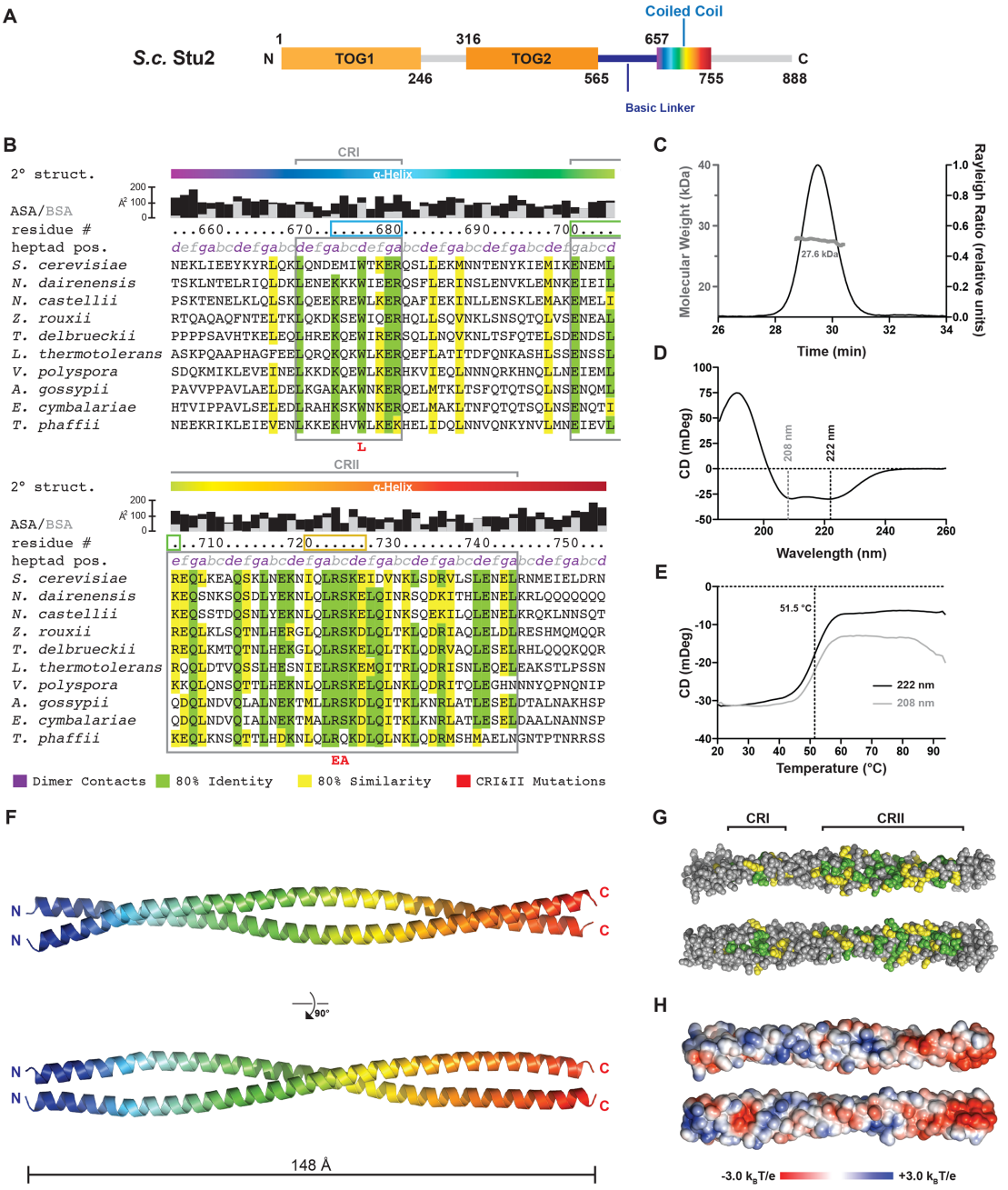

FIGURE 1: The Stu2 C-terminal domain is a dimeric coiled coil with two conserved regions. (A) Stu2 domain architecture, showing the two N-terminal TOG domains (TOG1 and TOG2, shown in light and dark orange, respectively), a central basic linker region implicated in microtubule binding (dark blue), and the C-terminal coiled-coil domain (rainbow). (B) Sequence alignment of the $Stu2_{CC}$ region across diverse yeast species. Residues with 80% identity and 80% similarity are highlighted in green and yellow, respectively. Conserved regions (CRI and CRII) are boxed and point mutations in these regions are indicated in red below the alignment. Residue numbers are indicated for Stu2. Heptad repeat positions are indicated in lowercase letters (*a*–*f*) above the alignment. Residues involved in the dimerization interface are colored magenta. The accessible surface area (ASA, black) and buried surface area (BSA, gray) for each residue in chain A is presented above the alignment, calculated using the ePISA server (Krissinel and Henrick, 2007). ASA is calculated based on the solvent accessibility of a residue in the absence of chain B and symmetry mates. Regions from the alignment shown in molecular detail in Figure 2, D–F, are boxed in cyan, green, and yellow, respectively. (C) SEC-MALS analysis of $Stu2_{CC}$. $Stu2_{CC}$ forms a dimer in solution at pH 7.5 with an experimentally determined molecular weight of 27.6 kDa vs. its 13.5-kDa formula weight. (D) CD spectra of $Stu2_{CC}$ (11 μM) at 23°C, showing minima at 208 and 222 nm, indicative of α-helical secondary structure. (E) CD thermal melt of $Stu2_{CC}$ monitoring CD signal at 208 nm (gray trace) and 222 nm (black trace). The inflection point of each melt curve occurs at 51.5°C. (F) Cartoon diagram of the $Stu2_{CC}$ structure with both chains colored in an indigo to red spectrum from the N-terminus to the C-terminus. Image below is after a 90° rotation about the *x*-axis. (G) The $Stu2_{CC}$ structure shown in spherical format, colored gray with conserved resides colored in green and yellow as in Figure 1B. (H) $Stu2_{CC}$ electrostatics, contoured from –3 k_BT/e (red) to +3 k_BT/e (blue). The two orientations of $Stu2_{CC}$ in G and H correlate with the orientations in F.

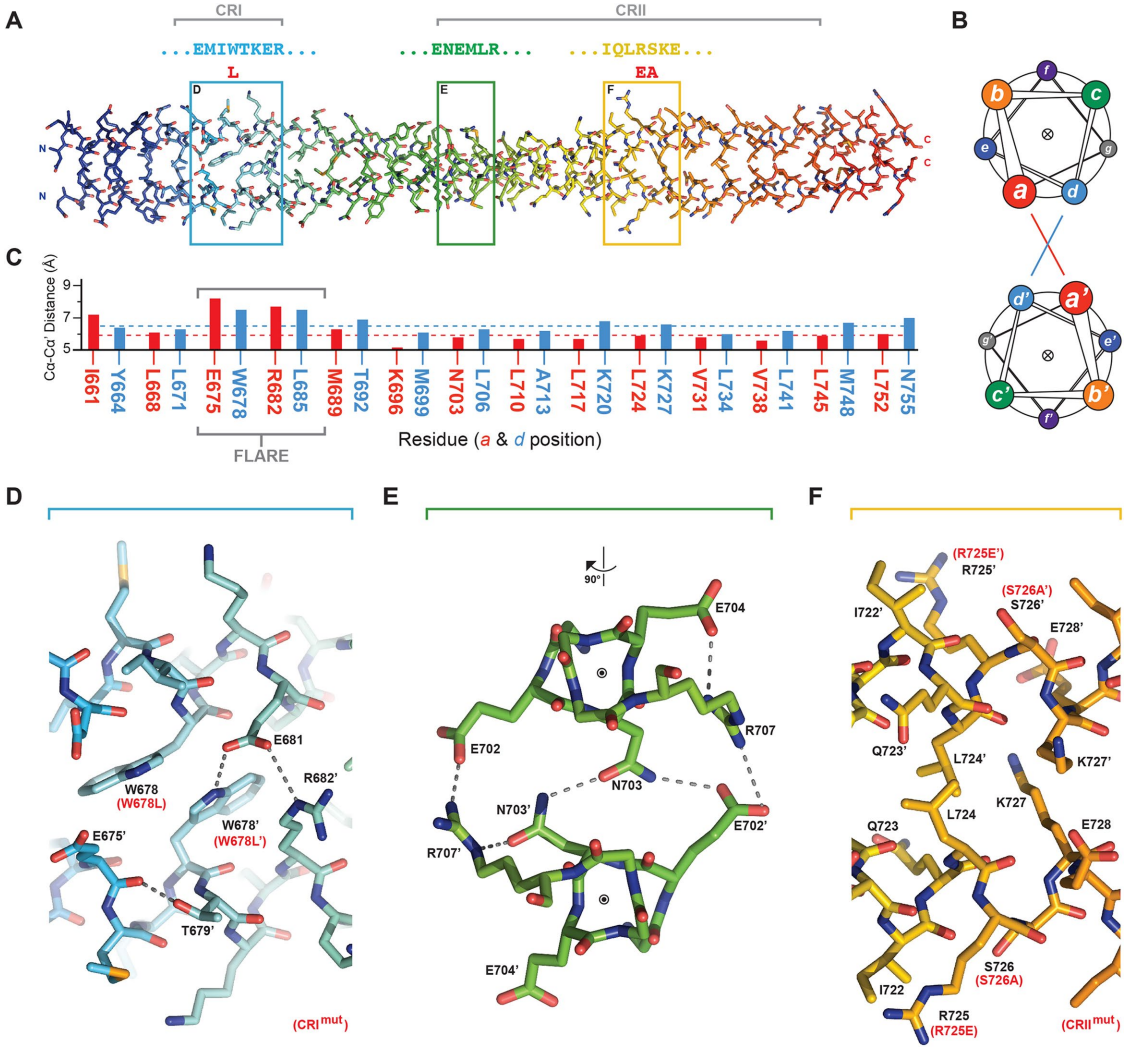

FIGURE 2: Stu2$_{CC}$ contains conserved and distinct structural features. (A) Stick diagram of the Stu2$_{CC}$ dimer, shown in an indigo to red spectrum from the N-termini to the C-termini. Regions shown in detail in D–F are boxed and their corresponding sequence is indicated at the top. (B) Standard homodimeric coiled-coil helical wheels showing the relative positions of heptad repeat residues *a* through *f* and *a*′ through *f*′. Positions *a*, *d*, *a*′, and *d*′ are located at the dimerization interface. (C) Interchain *a*–*a*′ (red) and *d*–*d*′ (cyan) distances (measured in Å) between homologous Stu2$_{CC}$ Cα atoms at the dimer interface are plotted. The asymmetric packing of the conserved W678 side chains underlies the helical flare that spans E675 to K688 (indicated). Red and cyan dashed lines represent the average Cα–Cα′ distance for the *a*–*a*′ (5.9 Å) and *d*–*d*′ (6.5 Å) measurements, respectively (averages were calculated excluding residues in the helical flare). (D) Zoom view of the CRI helical flare involving W678. W678 and W678′ are packed asymmetrically. W678′ is stabilized by a network of hydrogen bonds (dashed lines) involving the conserved residues E681 and R682′. An intrahelical hydrogen bond involving T679′ and the E675′ backbone carbonyl further stabilizes the region. Residues are shown in cyan stick format. (E) Zoom view of CRII spanning E702–R707 involving an extensive regional dimerization interface stabilized by a network of hydrogen bonds (dashed lines). Selected residues are shown in green stick format. Image is viewed out of the bore of the helices after a 90° rotation about the *x*-axis of the image shown in A. (F) Zoom view of the CRII segment containing the sequence LRSK (residues 724–727) shown in yellow stick format. The surface exposed R725 and S726 residues are not involved in dimer formation or intra- or interhelical hydrogen bonding. CRI and CRII residues mutated in this study are indicated in red in A, D, and F.

temperature (18°C) and/or benomyl treatment. (Figure 3A). In the absence of benomyl, all strains grew indistinguishably at 32° and 40°C. However, mutants placed at 18°C in the absence of benomyl displayed severe growth inhibition. Mutants also displayed enhanced benomyl sensitivity when grown on plates at 32° or 40°C or in liquid culture at 32°C (Figure 3, A–C). These results support a role for Stu2 CRI and CRII in regulating the microtubule cytoskeleton and cell division. In support, after overnight growth at 18°C, Stu2 CRI^{mut} and CRII^{mut} cells grew massive in size (>2 × WT) while WT Stu2-myc cells had no gross cellular defect (unpublished data).

We analyzed mutant Stu2$_{CC}$ constructs using SEC-MALS and CD to determine if the CRI and CRII mutations we introduced compromised the domain's stability or dimeric state. Stu2$_{CC}$ CRI^{mut} and Stu2$_{CC}$ CRII^{mut} each eluted as a single peak off a gel filtration column with an experimentally determined mass of 27.0 kDa, indicative of homodimerization (Figure 3, D and E). Each mutant also produced

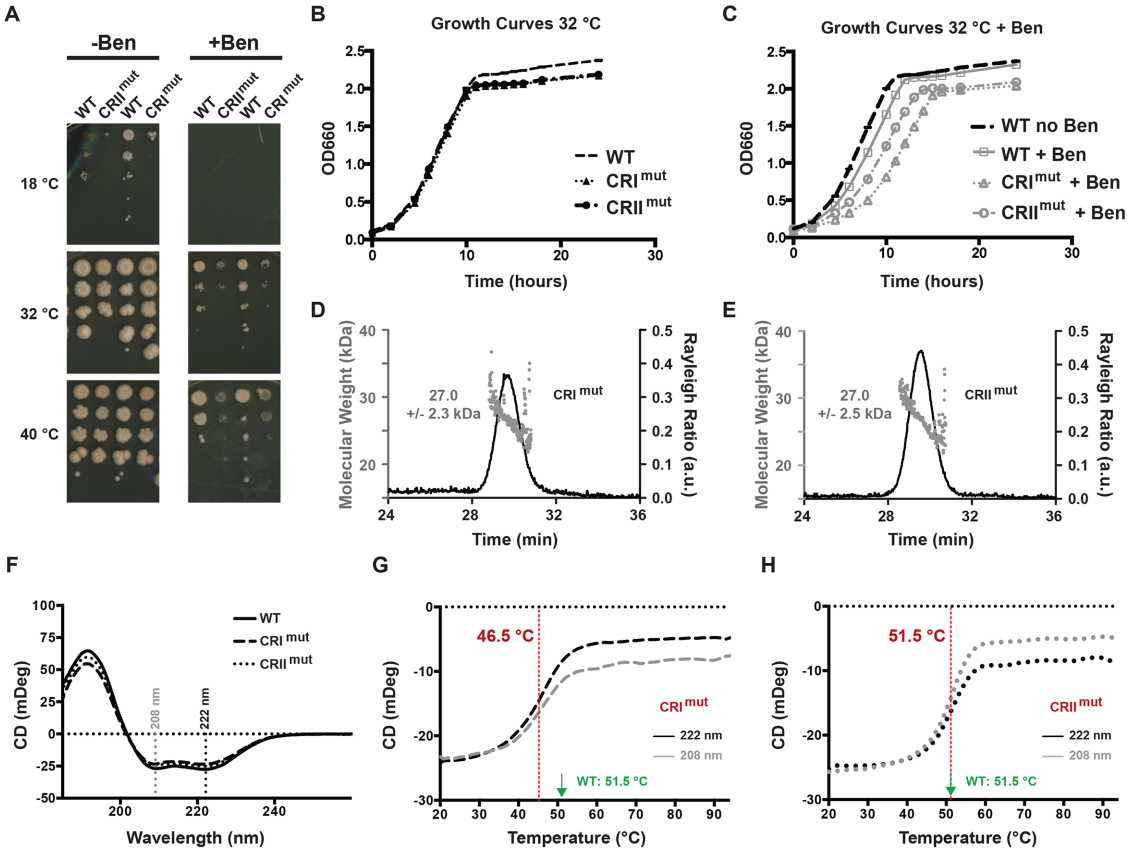

FIGURE 3: Mutations in Stu2$_{CC}$ CRI and CRII lead to increased benomyl and cold sensitivity. (A) Yeast strains (WT Stu2-myc, Stu2-myc-CRI^{mut}, and Stu2-myc-CRII^{mut}) were plated using a 10-fold serial dilution series on 0 or 10 µg/ml benomyl (Ben). Duplicate plates were put at 18°, 32°, and 40°C. Benomyl sensitivity is indicated by decreased growth at 32 and 40°C (no growth is observed even for WT yeast on benomyl plates at 18°C). Cold sensitivity is apparent for 18°C plates with no benomyl treatment. Data shown are representative of two independent experiments. (B) Yeast growth curves. Yeast strains were diluted to an OD_{660} of 0.1 in YPD and grown at 32°C shaking at 250 rpm. Growth curves plot OD_{660} over a 24-h time period. All strains grown in YPD at 32°C have similar growth rates. (C) Yeast strains were grown as in B, but YPD was supplemented with 10 µg/ml benomyl. Introducing benomyl slows the growth rate for both the CRI^{mut} and CRII^{mut} strains. Growth experiments shown in B and C are from a single experimental day and are representative of three experimental replicates. (D, E) SEC-MALS analysis of Stu2$_{CC}$ CRI^{mut} (D) and CRII^{mut} (E). Both constructs are homodimeric based on their experimentally determined masses. (F) CD spectra of WT and mutant Stu2$_{CC}$ constructs CRI^{mut} and CRII^{mut} at 23°C all show signature minima at 208 and 222 nm, indicative that the mutations do not perturb the domain's α-helical character. (G, H) CD thermal melts of mutant Stu2$_{CC}$ constructs CRI^{mut} (G) and CRII^{mut} (H). Stu2$_{CC}$ CRI^{mut} and CRII^{mut} have cooperative unfolding profiles with inflection points at 46.5 and 51.5°C, respectively. The CRI mutation W678L lowered the T_m by 5°C relative to the WT construct (see Figure 1E, 51.5°C, indicated in G and H by a green arrow). The CRII double mutations R725E and S726A did not change the T_m from the WT value. SEC-MALS and CD data are representative of two experimental replicates.

an α-helical CD spectrum with minima at 208 and 222 nm (Figure 3F). Thermal melt analysis gave apparent T_m values of 46.5°C for Stu2$_{CC}$-CRI^{mut} and 51.5°C for Stu2$_{CC}$-CRII^{mut} (Figure 3, G and H) that were similar to WT (51.5°C; Figure 1E). These results indicate that both mutants are stable and dimeric over the temperature range analyzed in vivo, giving us license to move forward with functional analyses.

Stu2 CRI and CRII determinants contribute to spindle morphology

We hypothesized that growth defects in the Stu2 CRI^{mut} and CRII^{mut} strains arose from mitotic failure. We introduced mCherry-Tub1 into our Stu2 strains and analyzed spindle morphologies at 32°C. Severe spindle defects were observed in the Stu2 CRI^{mut} and CRII^{mut} strains (Figure 4, A and B). Stu2 CRI^{mut} and CRII^{mut} strains had significantly more mispositioned spindles as compared with WT (CRI^{mut} = 43%, CRII^{mut} = 19%, WT = 6%). Unexpectedly, we observed many cells with fragmented spindles reminiscent of a temperature-sensitive *stu2* mutation (Severin *et al.*, 2001). While spindle fragmentation was not observed in WT cells, it was observed in CRI^{mut} cells with a frequency of 15% and in CRII^{mut} cells with a frequency of 27%. Collectively, abnormal spindles were observed in 58% of Stu2 CRI^{mut} mitotic cells, 46% of Stu2 CRII^{mut} mitotic cells, and only 6% of WT Stu2 mitotic cells. The higher percentage of aberrant spindles in the Stu2 CRI^{mut} strain correlates with a more pronounced growth defect under benomyl treatment (Figure 3C).

CRI and CRII determinants regulate Stu2 positioning and spindle structure

We next analyzed Stu2-GFP localization in CRI^{mut}, CRII^{mut}, and WT mitotic cells. Spindle poles were labeled using Spc29-RFP. In ~90% of WT Stu2-GFP mitotic cells, two Stu2-GFP foci appeared internal

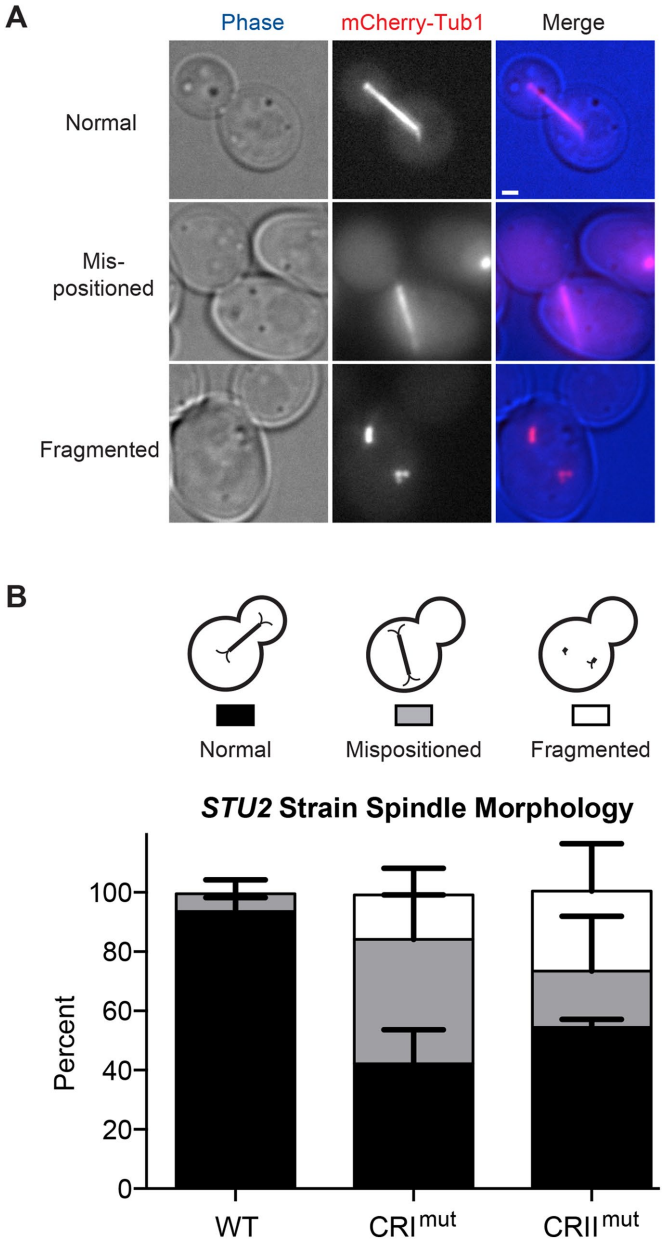

FIGURE 4: Mitotic spindle structure is disrupted in the Stu2-CRI^{mut} and Stu2-CRII^{mut} strains. (A) Representative images of spindle morphology phenotypes scored including normal, mispositioned, and fragmented spindles. Images taken are from the Stu2-CRII^{mut} strain grown at 32°C. Rows show phase, mCherry-Tub1, and merge. Scale bar is 1 µm. (B) Top: Cartoon representation of each mitotic spindle phenotype scored. Gray scale color correlates with the bars in the histogram shown at the bottom. Spindle morphologies were scored and binned for WT Stu2, Stu2-CRI^{mut}, and Stu2-CRII^{mut} strains. Stu2-CRI^{mut} and Stu2-CRII^{mut} strains have a significant increase in the frequency of aberrant spindle morphology (mispositioned or fragmented) as compared with the WT strain ($p < 0.005$; two-tailed unpaired Student's *t* test). Error bars represent SD ($n = 95$ [WT], 102 [CRI^{mut}], 85 [CRII^{mut}]). Data for each strain were collected across at least three independent experimental days.

to the two Spc29-RFP foci, correlating with the position of kinetochore microtubule (kMT) plus ends (Figure 5A). Surprisingly, the distribution and number of discreet Stu2-CRI^{mut}-GFP and Stu2-CRII^{mut}-GFP foci along the spindle axis was dramatically altered. Stu2-CRI^{mut}-GFP showed aberrant spindle localization in ~50% of mitotic cells, grown at either 18° or 32°C (Figure 5C). Stu2-CRII^{mut}-GFP showed aberrant spindle localization in 41% of mitotic cells grown at 32°C and 58% of mitotic cells grown at 18°C. When the Stu2 CRI^{mut} and CRII^{mut} GFP strains displayed two foci, the foci were anisotropically elongated along the spindle axis. Moreover, the amount of Stu2 on the spindle (integrated GFP fluorescence intensity) in foci directly proximal to the spindle pole body was significantly increased in the Stu2-CRI^{mut} and Stu2-CRII^{mut} strains compared with WT (Figure 5D). The dispersal of Stu2-CRI^{mut} and Stu2-CRII^{mut} along the spindle axis could compromise spindle dynamics, potentially leading to the fragmented and/or broken spindles observed in these strains. Overall, the mislocalization of mutant Stu2-GFP indicates a role for CRI and CRII in proper Stu2 kinetochore localization.

We next analyzed the effect of CRI and CRII mutations on metaphase spindle length and kinetochore positioning. No significant change in metaphase spindle length was observed at 32°C using Spc29-RFP as a pole marker. In contrast, metaphase spindle length was significantly longer in the mutant strains grown at 18°C (Stu2-CRI^{mut}: 1.18 µm, Stu2-CRII^{mut}: 1.25 µm) as compared with WT (0.89 µm) (Figure 5E). This may indicate that the mutants could not properly transition from metaphase to anaphase. In support, we observed a larger number of late metaphase spindles in the mutant *stu2* strains compared with WT (unpublished data). We inquired whether the Stu2 mutants compromised kinetochore organization using Ndc80-mCherry as a kinetochore marker. Neither mutant significantly perturbed the localization of Ndc80 at kinetochores, and sister kinetochore separation remained unchanged. Collectively, these data show that CRI and CRII play important roles in Stu2 localization, spindle architecture, and spindle dynamics.

DISCUSSION

We find that the Stu2$_{CC}$ domain forms a 15-nm parallel homodimeric coiled coil. This has implications for the relative positioning of the N-terminal TOG domains. Both TOG1 and TOG2 have αβ-tubulin binding activity and are required for Stu2's microtubule polymerase activity (Al-Bassam *et al.*, 2006; Slep and Vale, 2007; Ayaz *et al.*, 2012, 2014). The parallel coiled coil functionally permits the dimer's four TOG domains to drive microtubule polymerization in proximity to one another, potentially by promoting longitudinal and/or lateral tubulin:tubulin contacts. If the coiled coil was antiparallel, then the N-terminal TOG domain pairs would be spatially separated, limiting potential cooperative activity. Previous work using a monomeric TOG1-TOG2 construct that lacked the coiled coil formulated a TOG-dependent noncooperative tubulin-tethering mechanism that enhanced microtubule polymerization (Ayaz *et al.*, 2014). The Stu2$_{CC}$ structure primes the field to investigate whether full-length, dimeric Stu2 uses its four TOG domains to tether tubulin or to cooperatively bind tubulin and enhance lateral and/or longitudinal tubulin-tubulin interactions.

The Stu2$_{CC}$ structure highlights two conserved regions, CRI and CRII. CRI contains a conserved tryptophan (W678) that packs asymmetrically with its mate, causing a local flare in the coiled coil's diameter. A W678L mutation lowers the apparent T_m by 5°C, indicating that the W678–W678′ interface (potentially in the context of the flanking residues) provides enhanced stability to the coiled coil. The conserved nature of the CRI tryptophan and the structurally unique helical flare it causes suggests that this region may be a site for factor binding. The asymmetric packing of W678 and W678′ suggests that a binding factor may engage it in a 1:2 factor:Stu2 stoichiometry. This contrasts with CRII, which exhibits twofold

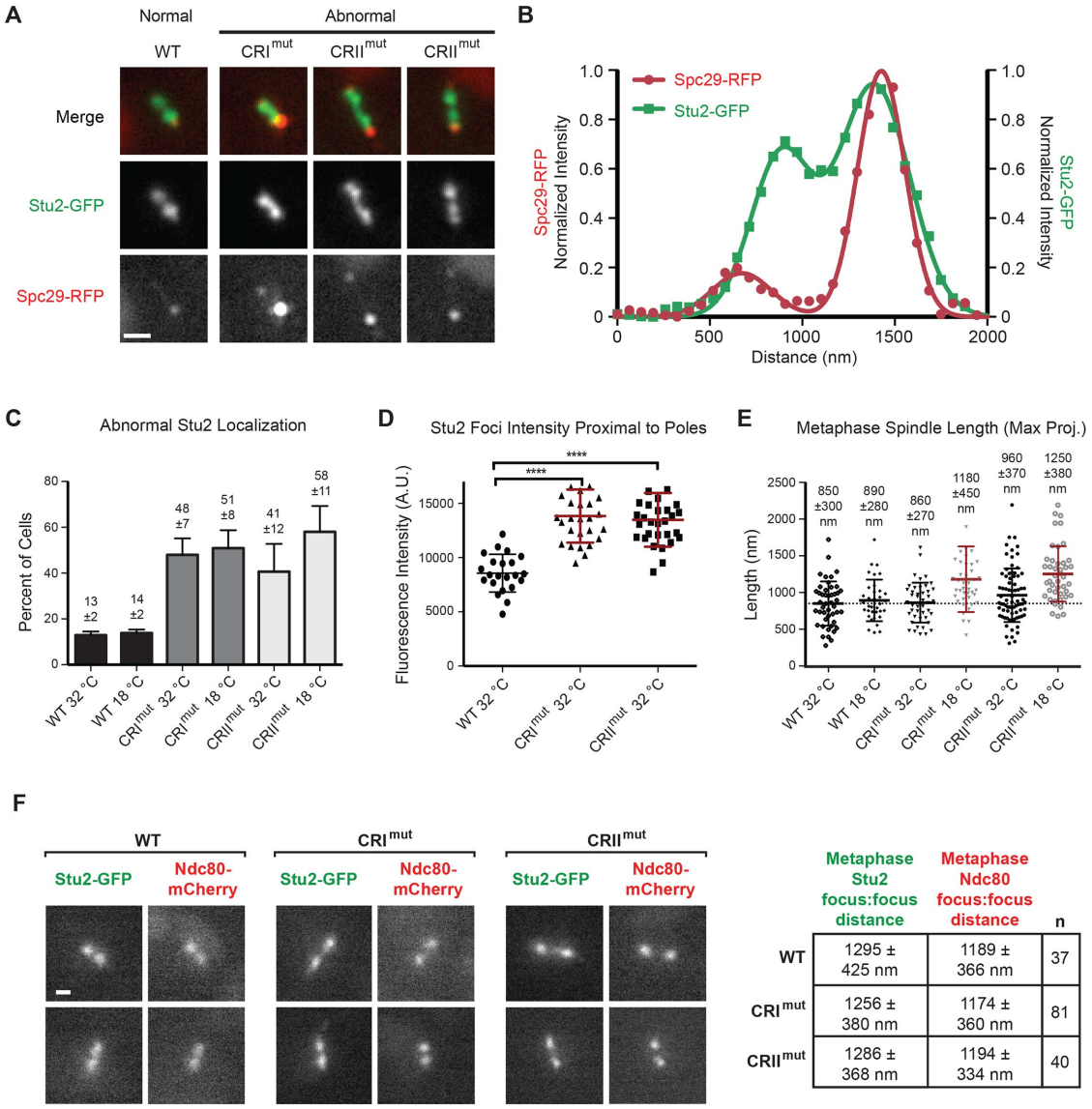

	Metaphase Stu2 focus:focus distance	Metaphase Ndc80 focus:focus distance	n
WT	1295 ± 425 nm	1189 ± 366 nm	37
CRI mut	1256 ± 380 nm	1174 ± 360 nm	81
CRII mut	1286 ± 368 nm	1194 ± 334 nm	40

FIGURE 5: Mutations in the Stu2$_{CC}$ CRI and CRII regions alter Stu2 distribution and localization on the yeast mitotic spindle and affect spindle length. (A) Stu2-GFP localizes to the metaphase mitotic spindle primarily as two foci, just interior to the Spc29-RFP foci that label the two spindle poles. Yeast grown at 32°C, scale bar: 1 μm. Mutant Stu2 strains CRI^{mut} and CRII^{mut} show altered distributions along the spindle. The Stu2-GFP CRI^{mut} and CRII^{mut} strains show defects in localization, including aberrant numbers of foci along the metaphase spindle. (B) Intensity line scan across a normal metaphase spindle shown in A. Two Spc29-RFP maxima define the mother (major peak) and daughter (minor peak) spindle pole bodies. Two WT Stu2-GFP foci localize just interior to the Spc29-RFP foci and are relatively uniform in intensity and distribution. (C) Quantification of Stu2-GFP localization to metaphase spindles between Spc29-RFP-labeled poles for strains grown at 32°C or grown at 32°C and shifted to 18°C for 1 h prior to imaging. Normal Stu2-GFP localization appears as two uniformly round foci as seen in A (left panel). Anything that deviated from this localization was classified as abnormal. Stu2-CRI^{mut} and CRII^{mut} strains had a significant increase in abnormal Stu2 localization relative to the WT strain at corresponding temperatures. (D) Stu2-GFP localization proximal to the spindle poles (32°C) is enhanced in the Stu2-CRI^{mut} and Stu2-CRII^{mut} strains. **** Indicates p value < 0.0001. (E) Stu2-CRI^{mut} and Stu2-CRII^{mut} strains show an increased apparent spindle length at 18°C. The black dotted line represents the WT mean at 32°C. All data with black errors bars are not statistically different from one another. The two gray scatter plots with red error bars indicate data that is statistically different from the black scatter plots (p value < 0.0001, two-tailed unpaired Student's t test) but not statistically different from one another. Scatter dot plots in D and E indicate the mean plus and minus the SD. (F) Ndc80-mCherry localization and foci separation are not perturbed in the Stu2-GFP CRI^{mut} and CRII^{mut} strains. Left: WT and mutant Stu2-GFP localization relative to Ndc80-mCherry foci. Right: mean distances between Stu2-GFP foci and Ndc80-mCherry foci for WT and mutant Stu2 strains. Yeast grown at 32°C, scale bar: 1 μm. Errors indicate SD. Data presented in C–F represent data collected from at least three independent experimental days per stain, per assay.

regional symmetry and likely engages binding factors in a 2:2 factor:Stu2 stoichiometry.

Structure-based mutagenesis within CRI and CRII has unveiled critical roles for the coiled coil in Stu2-dependent mitotic function. Mutating residues in either CRI or CRII compromised growth rates when yeast were challenged with cold or benomyl. Importantly, this was not because the mutations compromised Stu2 dimerization. Even in the absence of cold or benomyl treatment, these mutations led to an increased percentage of mispositioned and/or fragmented spindles and perturbed Stu2 localization along the spindle. While wild-type (WT) Stu2-GFP appeared as two foci along the spindle, CRI^{mut} and $CRII^{mut}$ constructs often appeared as multiple (>2) foci, anisoptropically distributed along the spindle axis. This localization pattern suggests an uncoupling of microtubule plus ends from kinetochores or a defocusing of the kinetochores. Analysis of Ndc80-mCherry localization in the Stu2 mutant strains did not reveal aberrant Ndc80 localization. This suggests that CRI and CRII determinants promote Stu2 kinetochore engagement and, when mutated, may uncouple microtubule plus ends from kinetochores. When yeast were challenged with cold (18°C), the metaphase spindle length increased in the CRI^{mut} and $CRII^{mut}$ strains but not in the wild-type strain. This suggests that a tension-sensing clutch mechanism, normally engaged in metaphase, became released in these mutants when challenged with cold. Recent work has identified Stu2/Dis1 as a Ndc80 complex binding factor involved in tension sensing (Measday *et al.*, 2005; Hsu and Toda, 2011; Tang *et al.*, 2013; Aravamudhan *et al.*, 2014; Miller *et al.*, 2016). Whether the Ndc80 complex engages CRI or CRII remains to be determined. Identifying the factors that do bind these regions will be critical for our understanding of kinetochore-microtubule attachment and dynamics. The $Stu2_{CC}$ structure we presented here and the conserved determinants we identified will be useful tools to resolve these questions.

MATERIALS AND METHODS

Cloning, expression, and purification of the Stu2 dimerization domain

STU2 DNA encoding residues 655–760 ($Stu2_{CC}$) was cloned from *Saccharomyces cerevisiae* genomic DNA into pET28 (Novagen, Millipore Sigma, St. Louis, MO) yielding an N-terminal, thrombin-cleavable H_6 tag. H_6-$Stu2_{CC}$ was expressed in BL21 DE3 (pLysS) *Escherichia coli* and induced using 0.1 mM isopropyl-1-thio-β-D-galactopyranoside (Teknova, Hollister, CA) at 18°C for 16 h. Cells were harvested, resuspended in lysis buffer (25 mM Tris, pH 8.0 [Fisher Chemical, Thermo Fisher Scientific, Waltham, MA], 300 mM sodium chloride [Fisher Chemical], 10 mM imidazole [Fisher Chemical], 0.1% β-mercaptoethanol [β-ME] [Acros Organics, Thermo Fisher Scientific]) and lysed by sonication. After lysis, phenylmethylsulfonyl fluoride (BioSynth, Wahlkreis of Rorschach, St. Gallen, Switzerland) was added to a final concentration of 1 mM. Lysate was clarified by centrifugation at 23,000 × *g*, and the supernatant loaded onto a Ni^{2+}-NTA (Qiagen, Venlo, Netherlands) column. H_6-$Stu2_{CC}$ was eluted using a 250-ml 10–300 mM imidazole gradient. Eluted protein was pooled, calcium chloride (Fisher Chemical) was added to 1 mM final concentration, and 0.125 mg bovine α-thrombin (Haematologic Technologies, Essex Junction, VT) was added to cleave the N-terminal H_6 tag. $Stu2_{CC}$ was filtered over 1 ml benzamidine sepharose (GE Healthcare, Marlborough, MA), exchanged into 25 mM Tris, pH 8.0, 0.1% β-ME using a Millipore Ultrafree 3k molecular weight cut-off concentrator, and loaded onto a Q Sepharose Fast Flow column (GE Healthcare). $Stu2_{CC}$ was eluted using a 0–1 M sodium chloride gradient over a 250-ml volume. Peak protein fractions were pooled, exchanged into storage buffer (25 mM Tris, pH 8.0, 100 mM sodium chloride, 0.1% β-ME), aliquoted, frozen in liquid nitrogen, and stored at -80°C. The final $Stu2_{CC}$ domain contained an N-terminal cloning artifact, residues: GSHM. Selenomethionine (SeMet) (Sigma Aldrich, St. Louis, MO)-substituted $Stu2_{CC}$ was produced in B834 *E. coli* as described previously (Leahy *et al.*, 1994) and purified as described above for the native construct.

Size exclusion chromatography–multi-angle light scattering

A 100-µl sample of 45 µM $Stu2_{CC}$ was injected onto a Superdex 200 10/300 GL gel filtration column (GE Healthcare) in 25 mM HEPES, pH 7.5 (Calbiochem, MilliporeSigma, St. Louis, MO), 300 mM sodium chloride, 0.1% β-ME, 0.2 g/l sodium azide (Fisher Chemical) and run in-line with a Wyatt DAWN HELIOS II light scattering instrument and a Wyatt Optilab T-rEX refractometer (Wyatt Technology Corp., Goleta, CA). Molecular weight was calculated with light scattering and refractive index data using the Wyatt Astra V software package (Wyatt Technology Corp.). SEC-MALS data presented are representative of experiments conducted in duplicate.

Circular dichroism

Circular dichroism spectra of $Stu2_{CC}$ WT and mutant constructs were collected at room temperature (23°C) using a Chirascan-plus CD spectrometer (Applied Photophysics, Leatherhead, UK). $Stu2_{CC}$ constructs were diluted to a final concentration of 11 µM in 10 mM sodium phosphate buffer (pH 7.5) (Fisher Chemical), 50 mM sodium fluoride (Fisher Chemical). Spectra were recorded from 260 to 185 nm with a step size of 0.5 nm using a 1-mm-path-length cuvette. The time per point was kept at 1.25 s. A base-line CD spectrum of the buffer alone was taken and subtracted from each $Stu2_{CC}$ spectrum. Spectra were smoothed in the Chirascan-plus software. CD melt spectra were obtained, monitoring 208 and 220 nm in 1°C steps from 20–94°C, with the time per point maintained at 1.25 s. CD data presented are representative of experiments conducted in duplicate.

Crystallization

Stu2 crystals were obtained by hanging drop vapor diffusion using 2 µl of purified SeMet-substituted $Stu2_{CC}$ (20 mg/ml stock) and 2 µl of the 1-ml well solution: 13% polyethylene glycol 8000 (Honeywell Fluka, Morris Plains, NJ), 200 mM magnesium acetate (Fisher Chemical), 100 mM sodium cacodylate, pH 5.75 (Fisher Chemical). Crystals grew at 20°C into thin, individual needles over a 1-wk period. Crystals were transferred into paratone-N (Hampton Research, Aliso Viejo, CA) and flash frozen in liquid nitrogen.

Diffraction data collection, structure determination, and refinement

Diffraction data were collected on a single SeMet-$Stu2_{CC}$ crystal at the Advanced Light Source beamline 8.3.1 at 100 K with 1° oscillations over 360° from a single crystal. Data were indexed, integrated, and scaled using HKL2000 (Otwinowski and Minor, 1997). The structure was determined using the AutoSol program (PHENIX crystallographic suite; Adams *et al.*, 2010). Ten selenium sites were identified in the heavy atom search in space group $P2_1$, accounting for the 10 ordered SeMet residues in the asymmetric unit. The model was built using AutoBuild (PHENIX; Adams *et al.*, 2010) and refined iteratively through manual builds in Coot (Emsley *et al.*, 2010) followed by refinement runs using phenix.refine (PHENIX; Adams *et al.*, 2010). Refinement statistics were monitored using a R_{free}, calculated using 10% of the data, randomly excluded from refinement (Brünger, 1992). Refinement runs utilized a maximum-likelihood Hendrickson Lattman target function. The final model includes two

Stu2 chains (chain A: residues 657–755; chain B: residues 658–755) and 25 water molecules. Crystallographic data and refinement statistics are presented in Supplemental Table S1. Atomic coordinates for the $Stu2_{CC}$ structure have been deposited to the PDB under accession code 6BL7.

Generation of *STU2* targeting plasmids

A DNA fragment of *STU2* corresponding to residues 357–888 was amplified from wild-type genomic DNA using a forward primer flanked with a *Bam*HI site and a reverse primer flanked with a *Hin*dIII site. The PCR product was digested with *Bam*HI and *Hin*dIII (New England Biolabs, Ipswich, MA) and cloned into a *pFA6-13x-myc::NAT* vector yielding a targeting plasmid with *STU2-357-888-13x-myc::NAT*. Within the targeting vector, specific point mutations (W678L or R725E, S725A) were introduced using site-directed mutagenesis and verified by sequencing. Primers to amplify and target the engineered *STU2* sequence to the endogenous locus were designed using homology-flanking arms of sequence just upstream of Stu2 residue 357 and just downstream of the *STU2* STOP codon. A similar protocol was used to generate *STU2* strains with a C-terminal GFP tag and *HIS* selection. Western blot analysis was used to confirm normal expression levels of Stu2 in the WT and mutant *STU2-13x-myc* strains generated.

Generation of *STU2* yeast strains

All strains in this study use YEF473A as the parental strain. PCR product with homology arms was gel extracted and transformed into competent WT yeast cells. *NAT*- or *HIS*-positive isolates were screened using a forward primer 401 base pairs upstream and a reverse primer 499 base pairs downstream of the *STU2* coding sequence. Isolates containing the integration at the genomic locus were confirmed by PCR. Two positive isolates from each desired background (*WT-STU2-13x-myc*, *STU2-W678L-13x-myc*, *STU2-R725E-S725A-13x-myc*, *WT-STU2-GFP*, *STU2-W678L-GFP*, and *STU2-R725E-S725A-GFP*) were chosen to move forward with functional analyses. PCR product amplified off of genomic DNA was sent for sequencing to verify introduction of the desired mutation(s). To visualize spindles, *pRS305:MET3p:mCherry-TUB1* (a gift from Wei-Lih Lee, Department of Biological Sciences, Dartmouth College, Hanover, NH) was digested with *Hin*dIII (New England Biolabs) and transformed into the *STU2-13x-myc* strains (Markus *et al.*, 2009). Strains were screened using fluorescence microscopy to confirm integration of the plasmid (Markus *et al.*, 2009). To determine Stu2 localization relative to the spindle pole body and the kinetochore, we generated independent *STU2-GFP* strains with either Spc29 (spindle pole body component; Elliott *et al.*, 1999) tagged at the C-terminus with RFP or Ndc80 (kinetochore component) tagged at the C-terminus with mCherry using a PCR cassette (Longtine *et al.*, 1998). Yeast strains used and generated in this study are presented in Supplemental Table S2.

Growth curves of yeast and benomyl sensitivity (liquid culture)

Yeast strains were diluted into either yeast extract–peptone–dextrose (YPD) or YPD + 10 µg/ml benomyl (Sigma Aldrich) to an OD_{660} of 0.1 from an overnight culture. These cultures were placed at 32°C, shaking at 250 rpm. The OD_{660} was measured every 1–2 h. Cell culture density over time was plotted in Sigma Plot (Systat Software, San Jose, CA).

Yeast plate growth assays

Tenfold serial dilutions of overnight yeast cultures were pronged onto plates containing 0 and 10 µg/ml benomyl. Two replicate plates were put at 18°, 32°, and 40°C. Cells were allowed to grow on plates for 3–5 d. Each plate was scanned on day 3 and day 5. Images shown in Figure 3A are after 5 d.

Imaging and image analysis

All strains were imaged on a Nikon TE-2000E (Nikon Instruments, Melville, NY) inverted microscope with a 1.43 NA, 100× Plan-Apo objective controlled by Metamorph software (Molecular Devices, Sunnyvale, CA). Cells were grown shaking in liquid culture in log phase at 32°C. One hour prior to imaging, cells were either maintained at 32°C or shifted to 18°C. Two Stu2-GFP foci along a spindle axis were characterized as normal Stu2 localization, aberrant Stu2 localization was classified as either the loss of two distinct GFP foci resulting in one large focus or a line of Stu2-GFP fluorescence along the spindle or more than two foci that were at least 1/3 the intensity of Stu2-GFP at the kinetochores. Distances between foci were determined using Gaussian fits as described (Haase *et al.*, 2013). Stu2 focus intensity was determined by integrating background-subtracted intensities in a 9×9 pixel region of interest centered on the respective pole-proximal Stu2-GFP focus. Metaphase spindle length was determined from max projections by measuring the distance between metaphase spindle poles using Spc29-RFP as a marker. Accordingly, the spindle length measurement presented is the apparent length based on the max projection. Only spindles that had two resolvable Spc29-RFP foci were used for this analysis. Any collapsed spindles (where two foci could not be independently resolved) were not included in these measurements. Imaging for all yeast strains was conducted across at least three separate experimental days per assay. Mitotic cells were chosen for image analysis. Sample size was chosen to ensure a high theoretical statistical power (greater than 90%) to generate reliable *p* values.

ACKNOWLEDGMENTS

We thank Ashutosh Tripathy for technical assistance and Wei-Lih Lee for the *pRS305:MET3p:mCherry-TUB1* plasmid. This work was supported, in whole or in part, by National Institutes of Health grants R01GM094415 (to K.C.S.), R37GM32238 (to K.B.), and T32GM008570 (to the UNC Molecular and Cellular Biophysics Program) and March of Dimes grant FY14-247 (to K.C.S.).

REFERENCES

Adams PD, Afonine PV, Bunkóczi G, Chen VB, Davis IW, Echols N, Headd JJ, Hung L-W, Kapral GJ, Grosse-Kunstleve RW, *et al.* (2010). PHENIX: a comprehensive Python-based system for macromolecular structure solution. Acta Crystallogr D Biol Crystallogr 66, 213–221.

Al-Bassam J, van Breugel M, Harrison SC, Hyman A (2006). Stu2p binds tubulin and undergoes an open-to-closed conformational change. J Cell Biol 172, 1009–1022.

Aravamudhan P, Felzer-Kim I, Gurunathan K, Joglekar AP (2014). Assembling the protein architecture of the budding yeast kinetochore-microtubule attachment using FRET. Curr Biol 24, 1437–1446.

Ayaz P, Munyoki S, Geyer EA, Piedra F-A, Vu ES, Bromberg R, Otwinowski Z, Grishin NV, Brautigam CA, Rice LM (2014). A tethered delivery mechanism explains the catalytic action of a microtubule polymerase. eLife 3, e03069.

Ayaz P, Ye X, Huddleston P, Brautigam CA, Rice LM (2012). A TOG:mbling the protein architecture of the budding yeast kinetochore-microtubule attachment using. FRET Curr 337, 857–860.

Brittle AL, Ohkura H (2005). Mini spindles, the XMAP215 homologue, suppresses pausing of interphase microtubules in *Drosophila*. EMBO J 24, 1387–1396.

Brünger AT (1992). Free R value: a novel statistical quantity for assessing the accuracy of crystal structures. Nature 355, 472–475.

Burkhard P, Kammerer RA, Steinmetz MO, Bourenkov GP, Aebi U (2000). The coiled-coil trigger site of the rod domain of cortexillin I unveils a distinct network of interhelical and intrahelical salt bridges. Structure 8, 223–230.

Chen XP, Yin H, Huffaker TC (1998). The yeast spindle pole body component Spc72p interacts with Stu2p and is required for proper microtubule assembly. J Cell Biol 141, 1169–1179.

De Wulf P, McAinsh AD, Sorger PK (2003). Hierarchical assembly of the budding yeast kinetochore from multiple subcomplexes. Genes Dev 17, 2902–2921.

Elliott S, Knop M, Schlenstedt G, Schiebel E (1999). Spc29p is a component of the Spc110p subcomplex and is essential for spindle pole body duplication. Proc Natl Acad Sci USA 96, 6205–6210.

Emsley P, Lohkamp B, Scott WG, Cowtan K (2010). Features and development of Coot. Acta Crystallogr D Biol Crystallogr 66, 486–501.

Gandhi SR, Gierliński M, Mino A, Tanaka K, Kitamura E, Clayton L, Tanaka TU (2011). Kinetochore-dependent microtubule rescue ensures their efficient and sustained interactions in early mitosis. Dev Cell 21, 920–933.

Garcia MA, Vardy L, Koonrugsa N, Toda T (2001). Fission yeast ch-TOG/XMAP215 homologue Alp14 connects mitotic spindles with the kinetochore and is a component of the Mad2-dependent spindle checkpoint. EMBO J 20, 3389–3401.

Gard DL, Becker BE, Josh Romney S (2004). MAPping the eukaryotic tree of life: structure, function, and evolution of the MAP215/Dis1 family of microtubule-associated proteins. Int Rev Cytol 239, 179–272.

Gard DL, Kirschner MW (1987). A microtubule-associated protein from *Xenopus* eggs that specifically promotes assembly at the plus-end. J Cell Biol 105, 2203–2215.

Haase J, Mishra P, Stephens AD, Haggerty R, Quammen C, Taylor RM II, Yeh E, Basrai M, Bloom K (2013). A 3D map of the yeast kinetochore reveals the presence of core and accessory centromere-specific histone. Curr Biol 23, 1939–1944.

He X, Rines DR, Espelin CW, Sorger PK (2001). Molecular analysis of kinetochore-microtubule attachment in budding yeast. Cell 106, 195–206.

Holm L, Rosenström P (2010). Dali server: conservation mapping in 3D. Nucleic Acids Res 38, W545–W549.

Hsu K-S, Toda T (2011). Ndc80 internal loop interacts with Dis1/TOG to ensure proper kinetochore-spindle attachment in fission yeast. Curr Biol 21, 214–220.

Kammerer RA, Schulthess T, Landwehr R, Lustig A, Engel J, Aebi U, Steinmetz MO (1998). An autonomous folding unit mediates the assembly of two-stranded coiled coils. Proc Natl Acad Sci USA 95, 13419–13424.

Kosco KA, Pearson CG, Maddox PS, Wang PJ, Adams IR, Salmon ED, Bloom K, Huffaker TC (2001). Control of microtubule dynamics by Stu2p is essential for spindle orientation and metaphase chromosome alignment in yeast. Mol Biol Cell 12, 2870–2880.

Krissinel E, Henrick K (2007). Inference of macromolecular assemblies from crystalline state. J Mol Biol 372, 774–797.

Leahy DJ, Erickson HP, Aukhil I, Joshi P, Hendrickson WA (1994). Crystallization of a fragment of human fibronectin: introduction of methionine by site-directed mutagenesis to allow phasing via selenomethionine. Proteins 19, 48–54.

Li W, Moriwaki T, Tani T, Watanabe T, Kaibuchi K, Goshima G (2012). Reconstitution of dynamic microtubules with *Drosophila* XMAP215, EB1, and Sentin. J Cell Biol 199, 849–862.

Longtine MS, McKenzie A, Demarini DJ, Shah NG, Wach A, Brachat A, Philippsen P, Pringle JR (1998). Additional modules for versatile and economical PCR-based gene deletion and modification in *Saccharomyces cerevisiae*. Yeast 14, 953–961.

Markus SM, Punch JJ, Lee W-L (2009). Motor- and tail-dependent targeting of dynein to microtubule plus ends and the cell cortex. Curr Biol 19, 196–205.

Measday V, Baetz K, Guzzo J, Yuen K, Kwok T, Sheikh B, Ding H, Ueta R, Hoac T, Cheng B, *et al.* (2005). Systematic yeast synthetic lethal and synthetic dosage lethal screens identify genes required for chromosome segregation. Proc Natl Acad. Sci USA 102, 13956–13961.

Miller MP, Asbury CL, Biggins S (2016). A TOG protein confers tension sensitivity to kinetochore-microtubule attachments. Cell 165, 1428–1439.

Nabeshima K, Kurooka H, Takeuchi M, Kinoshita K, Nakaseko Y, Yanagida M (1995). p93dis1, which is required for sister chromatid separation, is a novel microtubule and spindle pole body-associating protein phosphorylated at the Cdc2 target sites. Genes Dev 9, 1572–1585.

Nakaseko Y, Nabeshima K, Kinoshita K, Yanagida M (1996). Dissection of fission yeast microtubule associating protein p93Dis1: regions implicated in regulated localization and microtubule interaction. Genes Cells Devoted Mol Cell Mech 1, 633–644.

Otwinowski Z, Minor W (1997). Processing of X-ray diffraction data collected in oscillation mode. Methods Enzymol 276, 307–326.

Pearson CG, Maddox PS, Zarzar TR, Salmon ED, Bloom K (2003). Yeast kinetochores do not stabilize Stu2p-dependent spindle microtubule dynamics. Mol Biol Cell 14, 4181–4195.

Severin F, Habermann B, Huffaker T, Hyman T (2001). Stu2 promotes mitotic spindle elongation in anaphase. J Cell Biol 153, 435–442.

Slep KC, Vale RD (2007). Structural basis of microtubule plus end tracking by XMAP215, CLIP-170, and EB1. Mol Cell 27, 976–991.

Steinmetz MO, Stock A, Schulthess T, Landwehr R, Lustig A, Faix J, Gerisch G, Aebi U, Kammerer RA (1998). A distinct 14 residue site triggers coiled-coil formation in cortexillin I. EMBO J 17, 1883–1891.

Tang NH, Takada H, Hsu K-S, Toda T (2013). The internal loop of fission yeast Ndc80 binds Alp7/TACC-Alp14/TOG and ensures proper chromosome attachment. Mol Biol Cell 24, 1122–1133.

Usui T, Maekawa H, Pereira G, Schiebel E (2003). The XMAP215 homologue Stu2 at yeast spindle pole bodies regulates microtubule dynamics and anchorage. EMBO J 22, 4779–4793.

van Breugel M, Drechsel D, Hyman A (2003). Stu2p, the budding yeast member of the conserved Dis1/XMAP215 family of microtubule-associated proteins is a plus end-binding microtubule destabilizer. J Cell Biol 161, 359–369.

van der Vaart B, Manatschal C, Grigoriev I, Olieric V, Gouveia SM, Bjelic S, Demmers J, Vorobjev I, Hoogenraad CC, Steinmetz MO, *et al.* (2011). SLAIN2 links microtubule plus end-tracking proteins and controls microtubule growth in interphase. J Cell Biol 193, 1083–1099.

Wang PJ, Huffaker TC (1997). Stu2p: A microtubule-binding protein that is an essential component of the yeast spindle pole body. J Cell Biol 139, 1271–1280.